Journal of Magnetic Resonance 193 (2008) 243–250

Contents lists available at ScienceDirect

Journal of Magnetic Resonance

journal homepage: www.elsevier.com/locate/jmr

Inverting MRI measurements to heterogeneity spectra

Andrew E. Pomerantz *, Peter Tilke, Yi-Qiao Song

Reservoir Geosciences, Schlumberger-Doll Research, 1 Hampshire Street, Cambridge, MA 02139, USA

ARTICLE INFO

Article history:
Received 10 March 2008
Revised 8 May 2008
Available online 23 May 2008

Keywords:
MRI
Heterogeneity
Geostatistics
Porous media
Variogram
Heterogeneity spectrum
Heterogeneity spectra

ABSTRACT

Spatially resolved MRI measurements of porosity and relaxation time have been performed on a series of sandstone and carbonate rock cores in order to assess spatial heterogeneity in these samples. Geostatistical techniques such as the construction of experimental variograms provide a quantitative measure of heterogeneity, although the interpretation of standard techniques is at times ambiguous. Here, we attempt to resolve some of that ambiguity by addressing the influence of regularization (spatial averaging over the volume of a voxel) on the variogram. Modeling the influence of regularization allows measured variograms to be inverted, yielding a heterogeneity spectrum that shows the extent of spatial heterogeneity as a function of length scale. The current experiment is sensitive to heterogeneity on the 0.3–100 mm length scale, and heterogeneity spectra of carbonates are shown to vary widely from sample to sample over this range. Thus, this analysis is shown to provide a more detailed description of these porous media than the variogram or the first two moments of the porosity distribution provide. The magnetic resonance aspects of this technique are described here, while details of the geostatistical methodology are presented in a companion paper [A.E. Pomerantz, P.G. Tilke, Y.-Q. Song, Math. Geosci., submitted for publication].

1. Introduction

Investigations into the structure and dynamics of porous media are essential to many areas of physics and materials science [2]. It has long been understood that characterizing these materials and describing flow and transport in them is difficult due to their inherent heterogeneity. A situation in which transport through naturally heterogeneous porous media presents an important practical problem is found in the petroleum industry. There, subsurface flow of multiple phases through a variety of rock facies must be understood to identify petroleum reserves and ensure their efficient production. Particular interest lies in understanding fluid dynamics in carbonate rock formations. Carbonate sediments result from myriad biochemical process and suffer many diagenic changes between the time of their deposition and the time they are exploited as reservoir rocks [3–6]. These influences cause carbonate formations to be heterogeneous, to such an extent that well log interpretation models that were developed for and successfully applied to siliclastic formations are often unsuitable [6–8]. The petroleum industry is strongly motivated to understand these complex systems, as approximately 50% of proven oil reserves are contained in carbonate formations [6,7].

We are interested in developing methods to characterize heterogeneity in rock cores, with the goal being a measurement of the full heterogeneity spectrum, i.e., the extent of heterogeneity as a function of length scale over all relevant length scales. To accomplish this feat, it would be necessary for a measurement or combination of measurements to be able to probe large samples with fine resolution. Recent work with common imaging techniques, including microscopy and computed tomography, have focused on imaging at extremely high resolution [6,9–14]. The resolution attainable with these methods is often sufficient to distinguish individual pores and grains, making these techniques particularly appropriate for providing maps that can be used for lattice Boltzmann or pore network simulations [15,16]. However, porous media can be heterogeneous at length scales that exceed the maximum dimension observable with these high-resolution techniques, so high-resolution techniques alone are not always sufficient to characterize a material [10]. Our goal here is to describe a lower-resolution technique that complements these high-resolution techniques by providing a measurement of heterogeneity at length scales that are longer than the pore dimension but still very important to the structure of porous media.

MRI has the potential to perform such a measurement. While typically unable to resolve individual pores and grains, MRI is capable of lower-resolution imaging of samples that are relatively large. Additionally, magnetic resonance measurements have repeatedly been shown to provide useful petrophysical information, and NMR measurements are performed routinely in the oilfield [8,17–21]. For water-saturated rocks, CPMG measurements provide insight into the total porosity and distribution of pore sizes

* Corresponding author. Fax: +1 617 768 2386.
E-mail address: apomerantz@slb.com (A.E. Pomerantz).

1090-7807/$ - see front matter © 2008 Elsevier Inc. All rights reserved.
doi:10.1016/j.jmr.2008.05.014

[17,20,22–31]. The spatial resolution afforded by MRI can be used to extend these techniques from the bulk to permit measurement of the spatial variation of these petrophysically relevant quantities [30–46].

Previously we measured spatial distributions of porosity and relaxation, and, by comparing the spatially resolved results with spatially unresolved measurements, we developed a qualitative measurement of heterogeneity [47]. In that approach, relaxation times were measured for each voxel in the sample, and those measurements were combined to produce a relaxation time spectrum for the full core that could be compared to the more common relaxation time distribution measured with spatially unresolved NMR. It was shown that a comparison of these two spectra was sensitive to the extent of heterogeneity at different length scales. This qualitative measure of heterogeneity was used to show that heterogeneity both above and below the 1 mm length scale is important to the structure of carbonates.

The current goal is to create a quantitative method of interpreting these MRI experiments. A quantitative measurement should provide an elegant description of the importance of heterogeneity at different length scales and should be more informative than the simple presentation of spatial maps of porosity and relaxation time [12,48–53]. Here, a geostatistical analysis of MRI data is used to provide a quantitative measurement of the magnitude of heterogeneity at different length scales in carbonates and, for comparison, in more homogeneous sandstones. In this paper we describe the MRI measurement and briefly summarize a formalism showing how measurements performed at a particular resolution are sensitive to heterogeneity at different length scales. Using this technique, a generic spatially resolved measurement can be inverted to a heterogeneity spectrum over a certain range of length scales. This process is demonstrated using the MRI data, resulting in a heterogeneity spectrum for length scales on the order of 0.3–100 mm. Heterogeneity spectra are shown for carbonates and sandstones, highlighting the contrast between the two rock classes and demonstrating the application of the technique. Full details of the geostatistical techniques are provided in a companion paper [1].

2. Experimental methods

The samples measured in this study include several carbonate cores taken from a single Middle Eastern well over a depth range of 800 ft. Several sandstone samples were also measured. All rock cores were cut to 2 cm diameter and 3.75 cm length and were thoroughly cleaned and saturated with 0.20 Ωm NaCl brine. The carbonates contain mostly calcite and dolomite, have permeabilities in the range 0.4–4000 mD, and have full core porosities in the range 9–28 pu (individual voxel porosities span almost the full range 0–100 pu). The sandstones are similarly diverse, coming from multiple locations and having permeabilities in the range 0.5–2500 mD and full core porosities in the range 12–30 pu.

MRI experiments are performed at a 2-T magnetic field (Nalorac Cryogenics Corp., Martinez, CA) using an Avance™ console (Bruker BioSpin Gmbh) operating at 85 MHz. The experiments employ a multi-slice multi-echo (MSME) pulse sequence. This multi-slice phase-encoded spin echo imaging sequence effectively performs a CPMG experiment for each voxel. Cubic voxels of 1 mm length are used, and 100 echoes are collected at an echo time of 3.69 ms. The bandwidth of the refocusing pulse was set to be 50% greater than the bandwidth of the excitation pulse, and in order to avoid slice crosstalk, the slices were interleaved and a 0.5 mm gap was placed between adjacent slices; additionally, the recycle delay was set to 30 s to permit complete relaxation. The pulse durations are 0.970 ms for excitation and 0.410 ms for refocusing, and the phase-encoding gradient duration is also 0.410 ms. A 32×32 matrix is used, and 10 slices are recorded. The read bandwidth is 50 kHz, and the carbonates and sandstones measured here typically have linewidths near 100 Hz; paramagnetic materials in some sandstones can lead to linewidths an order of magnitude higher, at which point the resolution nears linewidth limitation. Experiments were signal averaged typically for 16 transients, which yielded a noise level of approximately 2 pu. Porosity maps for representative rocks are shown in Fig. 1.

2.1. Relaxation due to diffusion in the imaging gradients

Particular attention was paid to the effect of relaxation decay due to diffusion in the applied imaging gradients. It is desirable to image at high resolution in order to measure heterogeneity at short length scales and to use very short echo times in order to detect fast-relaxing spins and minimize decay due to diffusion in the internal field gradient [46]. Both of those goals require the application of intense magnetic field gradients. But, diffusion in these intense gradients makes its own contribution to the observed value T_2, and if this contribution is too large (i.e., if the imaging gradients are too strong) it will cause a systematic error in the measured relaxation time. Hence, the intensities and durations of the gradients and delays must be selected in a manner that balances good resolution and short echo time against minimizing systematic errors from relaxation due to diffusion in the imaging gradients.

The influence of diffusion in the imaging gradients on the observed T_2 is assumed to be described by

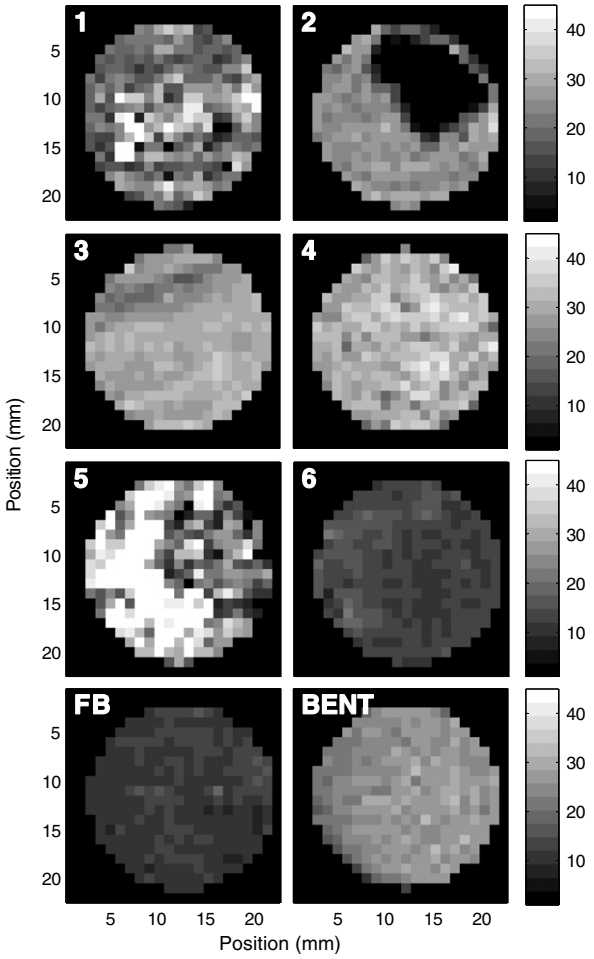

Fig. 1. Images of total porosity in units of pu. Images shown are 2-D slices through the center of the 3-D images. Cores identified by numbers are carbonates; "FB" stands for Fontainebleau sandstone; "BENT" stands for Bentheimer sandstone.

$$\frac{1}{T_{2,\mathrm{app}}} = \frac{1}{T_{2,\mathrm{int}}} + \frac{1}{T_{2,\mathrm{diff}}}, \tag{1.1}$$

where $T_{2,\mathrm{app}}$ is the apparent relaxation time; $T_{2,\mathrm{int}}$ is the intrinsic relaxation time, determined by bulk relaxation, surface relaxation, and diffusion in the internal gradient and reflecting the spin physics of the sample; and $T_{2,\mathrm{diff}}$ is the contribution due to diffusion in the imaging gradients. $T_{2,\mathrm{diff}}$ is computed by calculating the 3-D diffusion weighting from all the imaging gradients and assuming that the saturating water diffuses with its bulk self-diffusion constant [54]. $1/T_{2,\mathrm{diff}}$ can be minimized by minimizing the echo time, and the echo time in turn depends on the durations of the gradient and RF pulses [46].

The gradient and RF pulse durations are set to the minimum time available with the hardware. With those values minimized, the shortest echo time permitted by the hardware can be achieved; in this case, the shortest echo time is 3.69 ms. Having selected the echo time and the gradient timings and durations, $T_{2,\mathrm{diff}}$ can be calculated as a function of resolution (gradient strength). Increasing the resolution requires increasing the gradient strength, which in turn increases $1/T_{2,\mathrm{diff}}$. Even with this short echo time, $T_{2,\mathrm{diff}}$ can be significant. For example, in this experiment, we find $T_{2,\mathrm{diff}} = 8$ s using gradient strengths sufficient to achieve 1 mm isotropic resolution, but $T_{2,\mathrm{diff}} = 2.5$ s when using higher gradients as would be required to achieve 0.5 mm resolution. These carbonates samples are expected to contain some very large pores (vugs), in which $T_{2,\mathrm{int}}$ is approximately equal to the bulk relaxation time of water (around 3 s). Minimizing the systematic error in determining T_2 (i.e., achieving $T_{2,\mathrm{app}} \approx T_{2,\mathrm{int}}$) in those voxels then requires $T_{2,\mathrm{diff}} \gg 3$ *s*. Hence, 1 mm was selected as the highest achievable resolution.

In general, it should be noted that the systematic error produced by decay due to diffusion in the imaging gradients presents a fundamental limit to resolution achievable in these multiple spin echo experiments imaging T_2. The highest resolution that can be attained while still ensuring that the systematic error remains small depends on both the system hardware (for example, gradient switching time) and the sample (longest expected T_2). Relaxation due to diffusion in the imaging gradients generally cannot be fully corrected for in post-processing, as the (restricted) diffusion constant can vary spatially. The bulk self-diffusion constant used here represents the worst-case scenario; that value is useful for selecting a limiting resolution but cannot be used in a correction factor. These considerations must be kept in mind when selecting a resolution and echo time. In this case, 3.69 ms echo time and 1 mm isotropic resolution were chosen. In addition to these calculations, these parameters were shown to be adequate by using them to measure accurately the T_2 of water.

2.2. Data fitting

Relaxation decay in individual voxels is typically multiexponential, as has been observed previously [33–37]. Several options are available for fitting and analyzing these decay curves. Regularized numerical Laplace inversion is a popular technique for analyzing multiexponential decay curves because it is robust and can determine the full relaxation time distribution. However, this method has potential drawbacks. Noisy data require heavy regularization, resulting in features in the T_2 spectrum that are artificially broadened [55]. If less regularization is applied, the fit becomes unstable and many different T_2 spectra fit the data equally well. Additionally, sufficient echoes must be recorded such that high *S*/*N* data in the time domain persist for approximately as long as the relaxation time of the slowest decaying mode in the voxel. Such a measurement is possible, and Fig. 2 shows decays and T_2 spectra obtained by regularized Laplace inversion for three voxels of carbonate #1 [56]; these echo trains are recorded out to 900 ms or until the echo intensity drops below the 2 pu limit of detection. However, collecting relaxation data to long times and signal averaging until sufficient *S*/*N* is achieved often is prohibitively time consuming.

Fitting to a functional form with few adjustable parameters does not provide as detailed a solution as regularized Laplace inversion but is found to be a more appropriate alternative. Two common such functions are a stretched exponential and a multiexponential with only a small number of terms (typically 2 or 3) [33–37]. The multiexponential has the advantage that it can be physically interpreted in the same way as a T_2 spectrum from Laplace inversion, with relaxation times reflecting pore sizes and amplitudes reflecting the amount of water in those pores. Here, a double exponential was chosen to fit the decay in individual voxels:

$$\frac{M(t)}{M_0} = v_\mathrm{f} e^{-t/T_{2\mathrm{f}}} + v_\mathrm{s} e^{-t/T_{2\mathrm{s}}}. \tag{1.2}$$

This model contains four adjustable parameters: $T_{2\mathrm{f}}$ and $T_{2\mathrm{s}}$, representing the fast and slow decay time constants; and the weights v_f and v_s, representing the volumes of water in the different sized pores.

This model has several advantages. First, it typically fits the time domain data well, free of systematic errors resulting from too few adjustable parameters. Second, it can adequately fit relaxation times of seconds with only 370 ms of data collected in the time domain; even for voxels with the slowest relaxation, the error in determining $\log_{10} T_{2\mathrm{s}}$ is typically <0.05, which is an order of magnitude smaller than the typical width of the $T_{2\mathrm{s}}$ distribution for the core. Third, it is sufficiently flexible to provide a good description of the initial decay. Therefore, both the total voxel porosity, ϕ, and the average relaxation time, $\langle T_2 \rangle$, which corresponds to the initial decay rate, can be obtained by the following transformations involving parameters defined in Eq. (1.2):

$$\varphi = v_\mathrm{f} + v_\mathrm{s}. \tag{1.3}$$

$$\frac{\varphi}{\langle T_2 \rangle} = \frac{v_\mathrm{f}}{\langle T_{2\mathrm{f}} \rangle} + \frac{v_\mathrm{s}}{\langle T_{2\mathrm{s}} \rangle}. \tag{1.4}$$

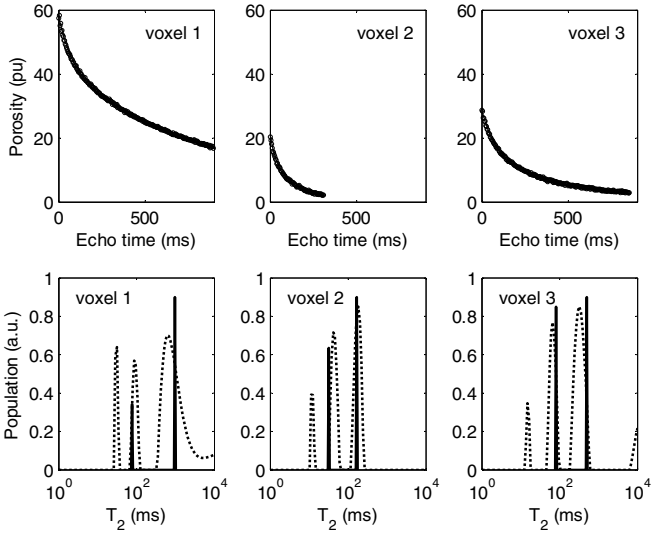

Fig. 2. Raw decays, fits, and T_2 spectra for three different voxels of carbonate #1. The top panel shows the raw decays (circles), along with the biexponential (solid line) and Laplace inversion (dashed line) fits. Both fits match the data quite well and are nearly indiscernible on this scale. The bottom panel shows arbitrarily normalized T_2 spectra. Results of the biexponential fit appear as delta functions in the T_2 spectra and capture the most important features of the Laplace inversion spectra.

Fig. 2 also shows the results of the biexponential fit for the selected voxels. The biexponential fit matches the experimental data throughout the decay, as shown in the top panels. Additionally, the parameters derived from the biexponential fit represent the salient features of the T_2 distribution, leading to the good agreement in the T_2 spectra shown in the bottom panel. The analysis presented below focuses on the spatial heterogeneity of ϕ and $\langle T_2 \rangle$, and the double exponential fit is sufficient to determine those quantities.

For some voxels, the measured decay is well described by a single exponential, and fits to a double exponential are unstable. The Akaike information criterion (AIC) [57] is used to determine if the double exponential, rather than a single exponential, is appropriate for fitting the data, as described in previous MRI work [47]. The AIC determines, in an information theoretical sense, whether or not a decrease in the mean squared error associated with fitting to a more complex function is sufficient to justify the use of the associated additional fitting parameters. Typically, the double exponential fit is justified in >90% of voxels. When the double exponential fit is not justified, the single exponential fit is retained, and ϕ and $\langle T_2 \rangle$ are taken to be the fitted porosity and relaxation time. Additionally, the fit was performed only for voxels with >4 porosity units (pu) initial signal. Only rarely did voxels not meet that criterion; for purposes of evaluating the heterogeneity, those voxels were assigned 2 pu total porosity and 5 ms relaxation time. Decay in individual voxels can also be fit to a triple exponential, and for data collected with the stated parameters, the S/N is such that the triple exponential fit is justified in only approximately half of the voxels. The four parameter double exponential fit is therefore preferred because that function is justified in almost every voxel and is still flexible enough to determine ϕ and $\langle T_2 \rangle$. However, it should be noted that a triple exponential is useful for detecting relaxation near 10 ms (representative of relatively small pores), which influences only the first few echoes at 3.69 ms echo time; bulk T_2 distribution measurements of these samples show only a minor contribution at this relaxation time.

3. Geostatistical analysis

3.1. Variograms

Quantitative results presented here are based on a geostatistical structural analysis of the MRI data. Detailed descriptions of geostatistics are found in Refs. [58,59], and a thorough description of this structural analysis is presented in the companion paper [1]. Here, we compute the two-point variogram, which measures the average squared difference between a parameter measured in two locations as a function of the vector separating those locations. For N pairs of measurements separated in space by the lag vector (h), the variogram $\gamma(h)$ is given by

$$2\gamma(h) = \frac{1}{N(h)} \sum_{i=1}^{N(h)} [z(x_i) - z(x_i + h)]^2, \tag{1.5}$$

where $z(x)$ is the quantity z measured at position x and the sum goes over all pairs of points separated by h [58,59]. For an ideal stationary random variable, the variogram is related to the covariance function (correlogram) by

$$\gamma(h) = \sigma^2 - \mathrm{Corr}(h), \tag{1.6}$$

where σ^2 is the variance of the parameter over the entire sample and $\mathrm{Corr}(h)$ is the correlogram [58]. For consistency with the majority of the geostatistical literature, we will discuss heterogeneity in terms of the variogram; similar arguments could be made in terms of the covariance function.

Variograms can be constructed for each parameter determined from the fit to individual voxels: $\varphi, v_f, v_s, \langle T_2 \rangle, T_{2f}, T_{2s}$, for a total of 6 variograms for each core. For simplicity, here we consider only ϕ and $\langle T_2 \rangle$. As the lag is a vector quantity, variograms can be computed along different directions to detect sample anisotropy. The rocks discussed here did not present any visually obvious signs of bedding or directionality, so cores were drilled in random directions. So, for these samples we will consider only isotropic variograms.

These variograms typically increase at small lags and then reach an asymptote at long lags. This behavior is interpreted as follows: the geology of the rock is such that a parameter (for example, porosity or T_2) rarely changes drastically from one region in space to another region a small distance away; that is to say, there is spatial correlation of the parameter. Hence, the average squared difference is small at short lags. At longer lags, drastic differences are more likely, resulting in an increasing variogram. At some point, the lag will exceed the maximum length scale of heterogeneity; at this point, increasing the lag no longer increases the mean squared difference, so the variogram will have reached its asymptotic value. If no asymptote is reached, that implies the existence of heterogeneity at length scales longer than the sample dimension, i.e., there is some trend or drift in the measured data (the problem is not stationary).

Variograms can be interpreted by fitting them to a model function. Several models exist to describe variograms with this appearance; for this study, the common exponential model is selected:

$$\gamma(h) = C_0 + C_1(1 - \mathrm{e}^{-h/a}). \tag{1.7}$$

In this model, C_0 is the nugget and represents heterogeneity at a length scale below the voxel dimension, i.e., heterogeneity on length scales nearly too small to be observed experimentally. $C_0 + C_1$ is the sill, or the asymptotic heterogeneity; for variograms with an asymptote, this parameter is typically similar to the total measured variance. The range a represents the characteristic length scale of heterogeneity that can be observed in the experiment (given the constraints of finite resolution and finite sample size). Experimental variograms of ϕ and $\langle T_2 \rangle$ for several carbonates and sandstones are presented in Figs. 3 and 4; parameters from the fit are summarized in Tables 1 and 2.

3.2. Heterogeneity spectra

Computed experimental variograms for porosity and $\langle T_2 \rangle$ provide quantitative information on the structure of porous media that is not available from the first two moments of the porosity distribution. Still, the question arises as to what exactly is the interpretation of the variogram. For example, only one length scale of heterogeneity is determined from the exponential fit to the variogram (and only a few length scales when the variograms can be fit to a nested structure), while the material may be heterogeneous over a large and continuous range of length scales; it is unclear how the length scale(s) extracted from the fit reflect this distribution of heterogeneity. Here, we give a brief description of how to define these terms more precisely and to relate quantitatively the measured variogram to the extent of heterogeneity on different length scales; a full description is provided in the companion paper [1].

Mathematically, we state this problem by considering a general porous medium with heterogeneity on many length scales, defined by an overall point variogram that is a nested structure consisting of a weighted sum of single length scale point variograms at different values of a (the characteristic length scale of heterogeneity):

$$\gamma_{\mathrm{tot}}(h) = \sum_i C_i \gamma(h; a_i). \tag{1.8}$$

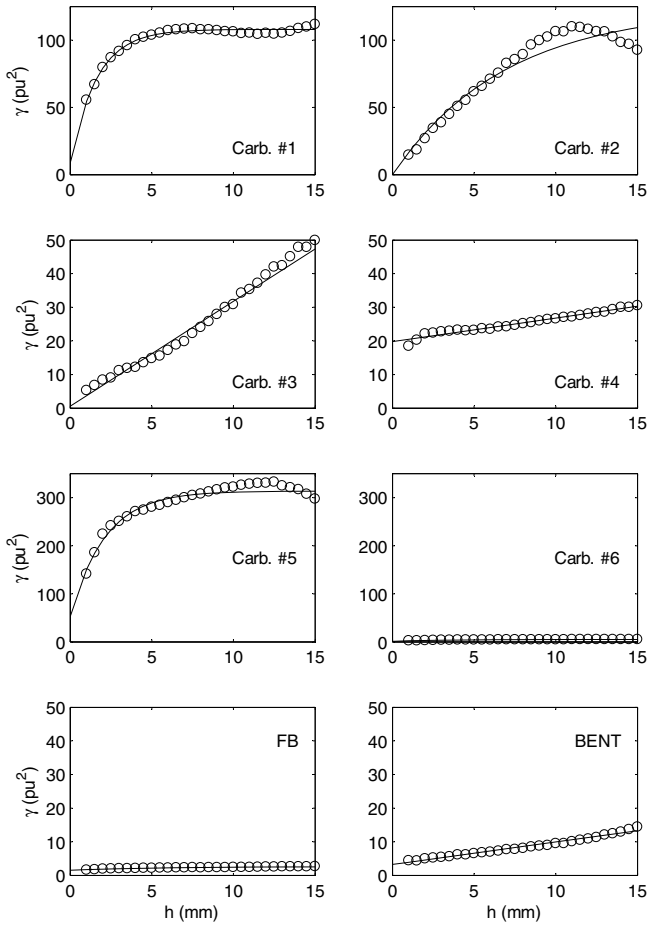

Fig. 3. Porosity variograms for the eight rocks. Labels are the same as in Fig. 1. Circles are the experimental variograms and lines are fits to the exponential model (Eq. (1.7)). The units of porosity are pu, so the units of γ are pu^2. For a proper comparison, both rocks in each row are presented with the same scale, and the sandstones are presented with the same scale as carbonates #3 and #4.

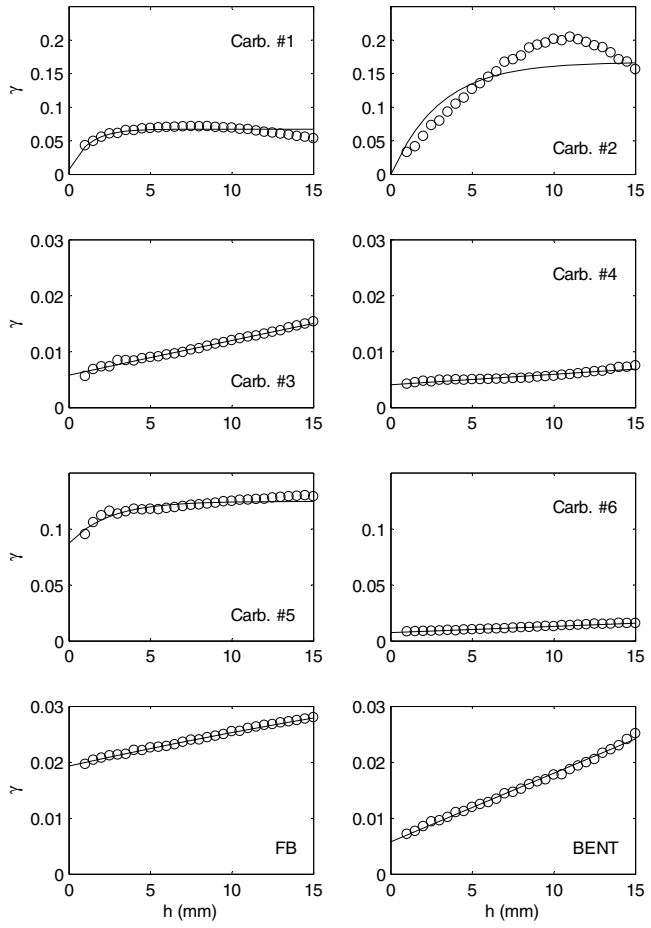

Fig. 4. $\langle T_2 \rangle$ variograms for the eight rocks. Labels are the same as in Fig. 1. Circles are the experimental variograms and lines are fits to the exponential model (Eq. (1.7)). Relaxation times are presented in the dimensionless form $\log_{10}(\langle T_2 \rangle/\text{ms})$, so the variograms are presented in that quantity squared. For a proper comparison, both rocks in each row are presented with the same scale, and the sandstones are presented with the same scale as carbonates #3 and #4.

$\gamma_{\text{tot}}(h)$ is the variogram defined on point support, meaning it is the true variogram that would be observed in a hypothetical measurement with zero noise and infinite resolution. The individual $\gamma(h;a_i)$ are the single length scale point variograms; in general, any suitable model variogram would suffice, and here we again chose the exponential model:

$$\gamma(h;a_i) = 1 - \text{e}^{-h/a_i}. \tag{1.9}$$

The C_i's represent the extent of heterogeneity at each length scale a_i. That is to say, a plot of C_i as a function of a_i is the heterogeneity spectrum we wish to present. Thus, the heterogeneity spectrum is similar to the more familiar power spectral density function, except that the heterogeneity spectrum inverts the variogram/correlogram with a Laplace transform to determine the length scales of decay, while the power spectral density function inverts the variogram/correlogram with a Fourier transform to determine the spatial frequencies of periodicity [60].

The experimental variogram differs from the point variogram in that the experimental variogram is regularized over the finite size of the voxel. The correct for this effect, the exponential model at a single length scale can be integrated over the finite volume of the voxel, resulting in a regularized model at a single length scale, $\gamma_{\text{v}}(h;a)$. In the overall regularized variogram, the exponential model functions are replaced by the regularized model functions:

$$\gamma_{\text{tot,v}}(h) = \sum_i C_i \gamma_{\text{v}}(h;a_i). \tag{1.10}$$

This overall regularized variogram corresponds to the variogram that is measured experimentally. For a finite number of length scales and measured lags, this relation can be shown in matrix form:

$$\gamma_{\text{tot,v}}(h) = \gamma_{\text{v}}(h;a)C(a), \tag{1.11}$$

where $\gamma_{\text{tot,v}}(h)$ is an m-element vector of measured points, $\gamma_{\text{v}}(h;a)$ is an $m \times n$ matrix relating the length scales of heterogeneity to points on the measured variogram, and $C(a)$ is an n-element vector representing the heterogeneity spectrum.

Using six length scales and the constraint that each element of C must be non-negative, Eq. (1.11) was solved for the porosity variograms; the resulting heterogeneity spectra $C(a)$ are shown in Fig. 5 (similar results for the $\langle T_2 \rangle$ variograms are not shown). The range of length scales of heterogeneity to which the measurement is sensitive is determined from the computed curves $\gamma_{\text{v}}(h;a)$; for this experimental geometry, the curves vanish for $a < 10^{-0.5}$ mm and $a > 10^2$ mm, so the appropriate range for this measurement is taken to be $10^{-0.5}$–10^2 mm. These heterogeneity spectra present the information from the variograms in a more easily interpretable manner, similar to how a T_2 spectrum is more interpretable than an echo train, or a chemical shift spectrum is more interpretable than an FID.

Table 1
Parameters of the porosity distributions and porosity variograms

Rock	ϕ (pu)	σ^2 (pu^2)	γ(1 mm) (pu^2)	C_0 (pu^2)	$C_0 + C_1$ (pu^2)	a (mm)
Carb #1	25	106	55	9	108	1.6
Carb #2	21	90	15	0	124	6.9
Carb #3	28	34	5	1	Drift	Drift
Carb #4	31	27	18	20	Drift	Drift
Carb #5	32	304	141	53	314	2.1
Carb #6	14	5	2	1	5	3.5
FB	12	2	2	2	3	5.4
BENT	26	11	4	3	Drift	Drift

ϕ and σ^2 are the first two moments of the porosity distribution. γ(1 mm) is the first measured point on the experimental variogram and is related to heterogeneity at short length scale. C_0, $C_0 + C_1$, and a are the results of fitting the variograms to the exponential model (Eq. (1.7)). When the variograms show no asymptote, there is a drift in the data so $C_0 + C_1$ and a cannot be determined.

Table 2
Parameters of the $\langle T_2 \rangle$ distributions and $\langle T_2 \rangle$ variograms

Rock	$\langle T_2 \rangle$	σ^2	γ(1 mm)	C_0	$C_0 + C_1$	a (mm)
Carb #1	1.75	0.063	0.043	0.007	0.067	1.2
Carb #2	1.64	0.166	0.033	0.000	0.167	3.0
Carb #3	1.27	0.012	0.006	0.006	Drift	Drift
Carb #4	1.77	0.006	0.004	0.004	Drift	Drift
Carb #5	2.01	0.124	0.095	0.088	0.125	2.4
Carb #6	1.58	0.013	0.008	0.008	Drift	Drift
FB	1.41	0.026	0.020	0.019	Drift	Drift
BENT	1.86	0.019	0.007	0.006	Drift	Drift

$\langle T_2 \rangle$ is presented throughout in the dimensionless measure $\log_{10}(\langle T_2 \rangle / \text{ms})$, so all elements in the table excluding a are dimensionless. $\langle T_2 \rangle$ and σ^2 are the first two moments of the $\langle T_2 \rangle$ distribution. γ(1 mm) is the first measured point on the experimental variogram and is related to heterogeneity at short length scale. C_0, $C_0 + C_1$, and a are the results of fitting the variograms to the exponential model (Eq. (1.7)). When the variograms show no asymptote, there is a drift in the data so $C_0 + C_1$ and a cannot be determined.

4. Results and discussion

4.1. Variograms

Figs. 3 and 4, along with Tables 1 and 2, show how the traditional variogram analysis can be used to quantify the diversity of heterogeneity found in sandstones and carbonates. In particular, it is found that the average porosity and the porosity variance are insufficient to describe these porous media; instead, the length scale of heterogeneity provides novel information that is needed for a more complete characterization. For example, carbonate #1 and carbonate #2 have similar average porosity and porosity variance, but their length scales of heterogeneity are quite different. Qualitatively, this effect can be seen by looking in the images in Fig. 1, where the image of carbonate #1 shows that adjacent voxels have very different porosities, indicating heterogeneity on a short length scale. The variogram expresses this quantitatively, as carbonate #1 has a short a and large γ(1 mm). The image of carbonate #2 shows one homogeneous region with 25–30% porosity and another homogenous region with very low porosity—the second region is composed of anhydrite and has virtually no NMR signal. The correlation length for this rock observed in the variogram is much longer than for carbonate #1 and approximates the size of the anhydrite feature, which is the dominant source of heterogeneity in this rock. Clearly the first and second moments of a rock's porosity distribution (the average porosity and porosity variance) do not suffice for detailed characterization of the rock. Additional information such as the heterogeneity length scale is required; this influence can be seen qualitatively in the images but is made quantitative with the variogram.

Another example is found in carbonates #3 and #4. These samples again have similar average porosity and porosity variance, and

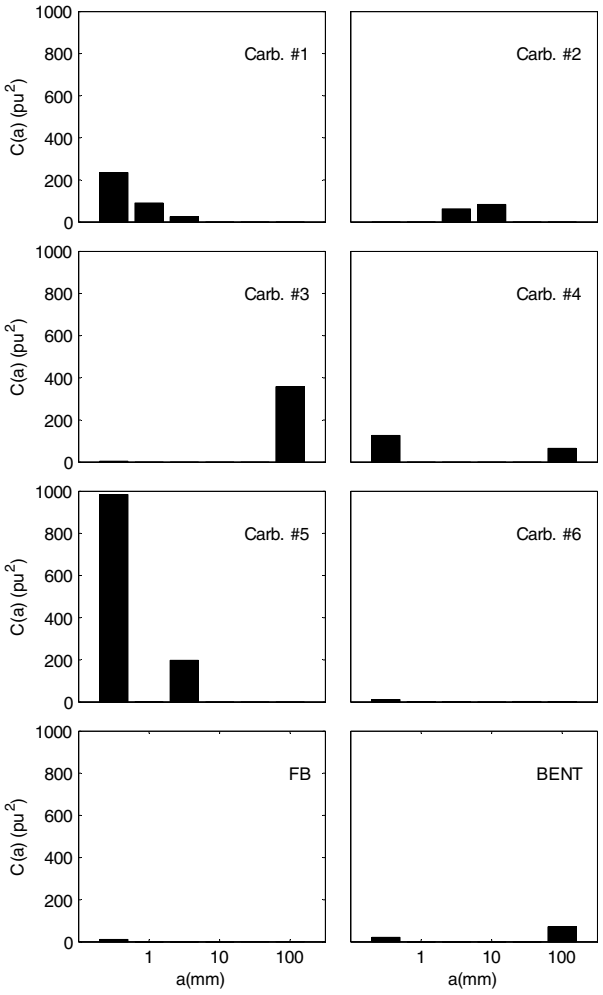

Fig. 5. Heterogeneity spectra for the eight rocks. Labels are the same as in Fig. 1. Both rocks in each row are presented with the same scale, and the sandstones are presented with the same scale as carbonates #3 and 4. See text for details.

in this case the porosity variograms never reach asymptotes. That asymptotes are not reached indicates the presence of heterogeneity on a length scale comparable to or exceeding the dimension of the sample; this can be seen clearly in the image of carbonate #3, where the low porosity feature in the top left of the image is as long as the sample itself. Because the variograms increase linearly with lag, it is impossible to determine a length scale of heterogeneity by fitting the variograms to an exponential function. Still, the variograms can provide quantitative information beyond the first two moments of the porosity distribution. In carbonate #4,

$\gamma(1\text{ mm})$ is already 65% of the porosity variance, indicating that most of the heterogeneity is present on small length scales approximating the voxel dimension. The variogram does not approach an asymptote because there also exists heterogeneity at much longer length scales, but the large value of $\gamma(1\text{ mm})$ compared to the variance (or equivalently, the shallow slope of the variogram) indicates that heterogeneity on those long length scales is relatively small. This contrasts with carbonate #3, where $\gamma(1\text{ mm})$ is only 15% of the variance, indicating that heterogeneity on the voxel scale is of limited importance. This quantitative analysis is consistent with the behavior that can be observed qualitatively just by looking at the images.

Carbonates #1–#4 are examples of how this technique can illuminate differences in heterogeneity among samples with similar macroscopic properties (i.e., mineralogy and porosity). The other samples give an example of differences between carbonates and sandstones. Carbonate #5 has a high porosity and is extremely heterogeneous, as shown by the variogram and the variance and also by direct viewing of the image. Carbonate #6 is shown on the same scale and is extremely homogeneous, as can be seen in the same measures. Thus, these cores illustrate the difference in heterogeneity that can occur in carbonates.

This result contrasts what is found for sandstones: the Fontainebleau and Bentheimer sandstones shown have different porosities but are both quite homogeneous, consistent with the general expectation. Similar results for Berea sandstones are not reproduced here. Thus, we find that sandstones are usually homogeneous, while the extent of heterogeneity in carbonates varies widely. The total variance of carbonate #6 is comparable to the variance of the sandstones, indicating that some carbonates can be as homogeneous as sandstones, while the variance for carbonate #5 is two orders of magnitude larger, demonstrating the extreme heterogeneity that can be found in carbonates.

While this discussion has focused on the porosity variograms, the same techniques can be applied to the relaxation time variograms. The $\langle T_2 \rangle$ variograms (Fig. 4) show the same gross features and overall trends as for the porosity variograms—e.g., carbonate #1 has a shorter characteristic length than carbonate #2, carbonate #5 has a higher variance than carbonate #6, etc. However, many of the details are different—e.g., the $\langle T_2 \rangle$variance for carbonate #2 is 2.5-fold larger than for carbonate #1, while the porosity variance is smaller. The observation implies that porosity and relaxation vary differently over the sample.

4.2. Heterogeneity spectra

The variograms presented in Figs. 3 and 4 provide quantitative information on the length scales of heterogeneity that extends the characterization of porous media beyond simply the first two moment of the porosity or relaxation time distribution. However, analyzing the variograms by fitting them to model functions is not completely satisfactory because the interpretation is ambiguous if many lengths of heterogeneity are present simultaneously. Heterogeneity spectra extended that analysis by resolving heterogeneity as a function of length scale. The heterogeneity spectra provide a new way to interpret the variograms, but strictly they do not contain any new information above the experimental variograms. The heterogeneity spectra of ϕ (Fig. 5) are shown below to provide more insight into the heterogeneity than the variograms of ϕ (Fig. 3), while the details from the heterogeneity spectra are consistent with the more coarse interpretation from fits to model functions.

Carbonate #1 presents heterogeneity on a shorter length scale than carbonate #2, as demonstrated roughly from the single exponential fit to the variogram by comparing the values of a. This result is shown in more detail in the heterogeneity spectrum, which peaks at 0.3 mm for carbonate #1 and at 10 mm for carbonate #2. Note that the measured length scale a from the single exponential fit (1.6 mm) is consistent with the heterogeneity spectrum (peaking at 0.3 mm), because a is regularized over the 1 mm voxel and the heterogeneity spectrum extracts the length scales of heterogeneity in the absence of regularization. The regularized range is approximately equal to the unregularized range plus the voxel dimension; that correction thus brings the range from the single exponential fit in accord with the heterogeneity spectrum [58].

Carbonate #3 shows heterogeneity exclusively at long length scales, consistent with the lack of asymptote in the variogram, while carbonate #4 shows mainly short length scale heterogeneity as well as some very long length scale heterogeneity, consistent with the large nugget and lack of asymptote in the variogram. Heterogeneity at the shortest length scale presented here ($10^{-0.5}$ mm) plays the role of the nugget, in agreement with the normal interpretation of the nugget. Finally, carbonate #5 is extremely heterogeneous and carbonate #6 is as homogeneous as the sandstones.

5. Conclusion

Spatially resolved measurements of porosity and relaxation time have been performed for carbonate and sandstone rock cores, and spatial heterogeneity has been assessed by constructing experimental variograms. The effects of finite regularization and sample size have been addressed, resulting in the $\gamma_v(h;a)$ functions that describe the sensitivity of each point on the experimental variogram to heterogeneity at different length scales. This allows the experimental variograms to be inverted, yielding the heterogeneity spectrum. Examples of heterogeneity spectra for carbonates and sandstones on the 0.3–100 mm range of length scales are presented in Fig. 5.

This measurement should prove useful in many regards. Most importantly, the heterogeneity spectrum allows for a quantitative interpretation of an experimental variogram by directly yielding the extent of heterogeneity as a function of length scale. Examples have been shown of rock cores with similar mineralogy, porosity, and porosity distributions that have very different heterogeneity spectra. Thus, the heterogeneity spectra provide novel information to characterize these samples in more detail than is possible with first two moments of the porosity distribution alone. Conclusions drawn from the heterogeneity spectrum are consistent with conclusions drawn from single exponential fits to the variograms, which are in turn consistent with conclusions drawn simply from looking at the images. However, these more detailed analyses provide more detailed and informative characterizations of the samples. Looking at the images allows one to gain a qualitative understanding of the gross features of the sample. Constructing the variogram and fitting to a single exponential yields quantitative information about heterogeneity on long and short length scales as well as a single value representing the most important length scale of heterogeneity. The heterogeneity spectrum provides much more detail by showing the heterogeneity at all length scales to which the measurement is sensitive. While the conclusions drawn from each of these analyses are consistent, the heterogeneity spectrum is clearly more enlightening than simple visual inspection of the images!

The MRI measurements presented here exemplify how the heterogeneity spectrum can be used. These measurements are sensitive to heterogeneity on the 0.3–100 mm length scale, and we find that these length scales are useful for distinguishing and characterizing reservoir rocks (i.e., these length scales are relevant to the structure of these samples); this is not necessarily the case at higher resolution [10]. Hence, the heterogeneity spectrum is used to provide a novel description of these samples. Using this technique, sandstones are

found to be mostly homogeneous on these length scales, in agreement with the general expectation. Carbonates, on the other hand, can be heterogeneous on many length scales, but they do not need to be; the heterogeneity of carbonates over the range 0.3–100 mm can vary widely from sample to sample. The analysis of individual samples and the resulting general trends demonstrate the utility of the heterogeneity spectrum in describing materials that are heterogeneous on multiple length scales.

Acknowledgment

The authors acknowledge Eric Sigmund for assistance with experiments and Wave Smith for assistance with sample preparation.

References

[1] A.E. Pomerantz, P.G. Tilke, Y.-Q. Song, Math. Geosci., submitted for publication.
[2] F.A.L. Dullien, Porous Media: Fluid Transport and Pore Structure, Academic Press, San Diego, 1992.
[3] F.J. Lucia, Carbonate Reservoir Characterization, Springer, Berlin, 1999.
[4] J. Grotzinger, T.H. Jordan, F. Press, R. Siever, Understanding Earth, fifth ed., W.H. Freeman and Co., New York, 2007.
[5] M.E. Tucker, Sedimentary Petrology: An Introduction to the Origin of Sedimentary Rocks, third ed., Blackwell Science, Oxford, 2001.
[6] C.H. Arns, F. Bauget, A. Limaye, A. Sakellariou, T.J. Senden, A.P. Sheppard, R.M. Sok, W.V. Pinczewski, S. Bakke, L.I. Berge, P.-E. Øren, M.A. Knackstedt, Pore scale characterisation of carbonates using X-ray microtomography, Soc. Petrol. Eng. (2004) 90368.
[7] R. Nurmi, E. Standen, Carbonates: the inside story, Middle East Well Eval. Rev. 18 (1997) 26–41.
[8] A. Adbel Latif, D. Sungur, I. Stockden, C. Cao Minh, Borehole nuclear magnetic resonance: experience and reservoir applications in West Kuwait carbonate reservoirs, Soc. Petrol. Eng. (1997) 37771.
[9] C. Lin, M.H. Cohen, Quantitative methods for microgeometric modeling, J. Appl. Phys. 53 (1982) 4152–4165.
[10] C. Lin, Microgeometry I: autocorrelation and rock microstructure, Math. Geol. 14 (1982) 343–359.
[11] P. Debye, H.R. Anderson Jr., H. Brumberger, Scattering by an inhomogeneous solid. II. The correlation function and its application, J. Appl. Phys. 28 (1957) 679–683.
[12] C.H. Arns, Presented at the SPWLA 48th Annual Logging Symposium, Austin, TX, 2007 (unpublished).
[13] P. Spanne, J.F. Thovert, C.J. Jacquin, W.B. Lindquist, K.W. Jones, P.M. Adler, Synchrotron computed microtomography of porous media: topology and transports, Phys. Rev. Lett. 73 (1994) 2001–2004.
[14] B.P. Flannery, H.W. Deckman, W.G. Roberge, K.L. D'Amico, Three-dimensional X-ray microtomography, Science 237 (1987) 1439–1444.
[15] N.S. Martys, J.G. Hagedorn, D. Goujon, J.E. Devaney, Presented at the Proceedings of SPIE: The International Symposium on Optical Science, Engineering, and Instrumentation, Denver, CO, 1999 (unpublished).
[16] R.M. Sok, M.A. Knackstedt, A.P. Sheppard, W.V. Pinczewski, W.B. Lindquist, A. Venkatarangan, L. Paterson, Direct and stochastic generation of network models from tomographic images; effect of topology on residual saturations, Transp. Porous Media 46 (2002) 345–372.
[17] W.E. Kenyon, Nuclear magnetic resonance as a petrophysical measurement, Nucl. Geophys. 6 (1992) 153–171.
[18] R. Freedman, N. Heaton, Fluid characterization using nuclear magnetic resonance logging, Petrophysics 45 (2004) 241–250.
[19] R. Freedman, Advances in NMR logging, J. Pet. Tech. (2006) SPE 89177.
[20] R.L. Kleinberg, Well logging, in: D.M. Grant, R.K. Harris (Eds.), Encyclopedia of Nuclear Magnetic Resonance, John Wiley & Sons, Chichester, 1996.
[21] D.V. Ellis, Well Logging for Earth Scientists, Elsevier, New York, 1987.
[22] K.R. Brownstein, C.E. Tarr, Importance of classical diffusion in NMR studies of water in biological cells, Phys. Rev. A At. Mol. Opt. Phys. 19 (1979) 2446–2453.
[23] R.L. Kleinberg, Pore size distributions, pore coupling, and transverse relaxation spectra of porous rocks, Magn. Reson. Imaging 12 (1994) 271–274.
[24] R.L. Kleinberg, W.E. Kenyon, P.P. Mitra, Mechanism of NMR relaxation of fluids in rock, J. Magn. Reson. Ser. A 108 (1994) 206–214.
[25] S. Davies, M.Z. Kalam, K.J. Packer, F.O. Zelaya, Pore-size distributions from nuclear magnetic resonance spin-lattice relaxation measurements of fluid-saturated porous solids. II. Applications to reservoir core samples, J. Appl. Phys. 67 (1990) 3171–3176.
[26] S. Davies, K.J. Packer, Pore-size distributions from nuclear magnetic resonance spin-lattice relaxation measurements of fluid-saturated porous solids. I. Theory and simulation, J. Appl. Phys. 67 (1990) 3163–3170.
[27] L.L. Latour, R.L. Kleinberg, A. Sezginer, Nuclear magnetic resonance properties of rocks at elevated temperatures, J. Colloid Interface Sci. 150 (1992) 535–548.
[28] K.J. Packer, Oil reservoir rocks examined by MRI, in: D.M. Grant, R.K. Harris (Eds.), Encyclopedia of Nuclear Magnetic Resonance, John Wiley & Sons, Chichester, 1996.
[29] S. Anferova, V. Anferov, D.G. Rata, B. Blümich, J. Arnold, C. Clauser, P. Blümler, H. Raich, A mobile NMR device for measurements of porosity and pore size distributions of drilled core samples, Concepts Magn. Reson. 23B (2004) 26–32.
[30] P.J. Barrie, Characterization of porous media using NMR methods, Annu. Rep. NMR Spectrosc. 41 (2000) 265–316.
[31] G.J. Hirasaki, NMR applications in petroleum reservoir studies, in: S. Stapf, S.-I. Han (Eds.), NMR Imaging in Chemical Engineering, Wiley-VCH, Weinheim, 2006.
[32] P.C. Lauterbur, Image formation by induced local interactions: examples employing nuclear magnetic resonance, Nature 242 (1973) 190–191.
[33] S. Chen, F. Qin, K.-H. Kim, A.T. Watson, NMR imaging of multiphase flow in porous media, in: Proceedings of the 67th Annual Technology Conference of the Society of Petroleum Engineers SPE #24760, 1992, pp. 1013–1026.
[34] J.J. Attard, T.A. Carpenter, L.D. Hall, S. Davies, M.J. Taylor, K.J. Packer, Spatially resolved T_1 relaxation measurements in reservoir cores, Magn. Reson. Imaging 9 (1991) 815–819.
[35] J.J. Attard, S.J. Doran, N.J. Herrod, T.A. Carpenter, L.D. Hall, Quantitative NMR spin-lattice-relaxation imaging of brine in sandstone reservoir cores, J. Magn. Reson. 96 (1992) 514–525.
[36] P.A. Osment, K.J. Packer, M.J. Taylor, J.J. Attard, T.A. Carpenter, L.D. Hall, N.J. Herrod, S.J. Doran, NMR imaging of fluids in porous solids, Philos. Trans. R. Soc. Lond. A 333 (1990) 441–449.
[37] M.R. Merrill, Porosity measurements in natural porous rocks using magnetic resonance imaging, Appl. Magn. Reson. 5 (1993) 307–321.
[38] G.C. Borgia, V. Bortolotti, P. Fantazzini, Changes of the local pore space structure quantified in heterogeneous porous media by ^{1}H magnetic relaxation tomography, J. Appl. Phys. 90 (2001) 1155–1163.
[39] G.C. Borgia, A. Brancolini, A. Camanzi, G. Maddinelli, Capillary water determination in core plugs: a combined study based on imaging techniques and relaxation analysis, Magn. Reson. Imaging 12 (1994) 221–224.
[40] W.A. Edelstein, H.J. Vinegar, P.N. Tutunjian, P.B. Roemer, O.M. Mueller, NMR imaging for core analysis, in: Proceedings of the 63rd Annual Technology Conference of the Society of Petroleum Engineers SPE #18272, 1988, pp. 101–112.
[41] F. Marica, Q. Chen, A. Hamilton, C. Hall, T. Al, B.J. Balcom, Spatially resolved measurement of rock core porosity, J. Magn. Reson. 178 (2005) 136–141.
[42] G. Guillot, C. Chardaire-Rivière, S. Bobroff, A. Le Roux, J.C. Roussel, L. Cuiec, Characterisation of wetting heterogeneities in sandstone rocks by MRI, Magn. Reson. Imaging 12 (1994) 365–368.
[43] M.K. Gingras, B. MacMillan, B.J. Balcom, Visualizing the internal physical characteristics of carbonate sediments with magnetic resonance imaging and petrography, Bull. Can. Pet. Geol. 50 (2002) 363–369.
[44] M.K. Gingras, B. MacMillan, B.J. Balcom, T. Saunders, S.G. Pemberton, Using magnetic resonance imaging and petrographic techniques to understand the textural attributes and porosity distribution in *Macaronichnus*-burrowed sandstone, J. Sediment. Res. 72 (2002) 552–558.
[45] Q. Chen, W. Kinzelbach, S. Oswald, Nuclear magnetic resonance imaging for studies of flow and transport in porous media, J. Environ. Qual. 31 (2002) 477–486.
[46] W.P. Rothwell, H.J. Vinegar, Petrophysical applications of NMR imaging, Appl. Opt. 24 (1985) 3969–3972.
[47] A.E. Pomerantz, E.E. Sigmund, Y.-Q. Song, Spatial heterogeneity length scales in carbonate rocks, Appl. Magn. Reson. 32 (2007) 221–231.
[48] M. Rotter, A. Berg, H. Langenberger, S. Grampp, H. Imhof, E. Moser, Autocorrelation analysis of bone structure, J. Magn. Reson. Imaging 14 (2001) 87–93.
[49] F.W. Wehrli, S.N. Hwang, J. Ma, H.K. Song, J.C. Ford, J.G. Haddard, Cancellous bone volume and structure in the forearm: noninvasive assessment with MR microimaging and image processing, Radiology 206 (1998) 347–357.
[50] J.G. Berryman, Measurement of spatial correlation functions using image processing techniques, J. Appl. Phys. 57 (1985) 2374–2384.
[51] C.H. Arns, J. Mecke, K. Mecke, D. Stoyan, Second-order analysis by variograms for curvature measures of two-phase structures, Eur. Phys. J. B 47 (2005) 397–409.
[52] G.A. Barrall, L. Frydman, G.C. Chingas, NMR diffraction and spatial statistics of stationary systems, Science 255 (1992) 714–717.
[53] P.J. Hicks Jr., H.A. Deans, K.R. Narayanan, Distribution of residual oil in heterogeneous carbonate cores using X-ray CT, SPE Formation Eval. 7 (1992) 235–240.
[54] E.M. Haacke, R.W. Brown, M.R. Thompson, R. Venkatesan, Magnetic Resonance Imaging: Physical Principles and Sequence Design, Wiley-Liss, New York, 1999.
[55] Y.-Q. Song, L. Venkataramanan, L. Burcaw, Determining the resolution of Laplace inversion spectrum, J. Chem. Phys. 122 (2005) 104104.
[56] Y.-Q. Song, L. Venkataramanan, M.D. Hürlimann, M. Flaum, P. Frulla, C. Straley, T_1–T_2 correlation spectra obtained using a fast two-dimensional Laplace inversion, J. Magn. Reson. 154 (2002) 261–268.
[57] H. Akaike, A new look at the statistical model identification, IEEE Trans. Auto. Cntl. 19 (1974) 716–723.
[58] A.G. Journel, C.J. Huijbregts, Mining Geostatistics, The Blackburn Press, Caldwell, NJ, 1978.
[59] E.H. Isaaks, R.M. Srivastava, An Introduction to Applied Geostatistics, Oxford University Press, New York, 1989.
[60] J.S. Bendat, A.G. Piersol, Random Data: Analysis and Measurement Procedures, John Wiley & Sons, New York, 1971.